Event texture search for phase transitions in Pb+Pb collisions

I. Bearden,[1] H. Bøggild,[1] J. Boissevain,[2] L. Conin,[4] J. Dodd,[3] B. Erazmus,[4] S. Esumi,[5,*] C. W. Fabjan,[6] D. Ferenc,[7] D. E. Fields,[2,†] A. Franz,[6,‡] J. J. Gaardhøje,[1] A. G. Hansen,[1,§] O. Hansen,[1] D. Hardtke,[9,‖] H. van Hecke,[2] E. B. Holzer,[6] T. J. Humanic,[9] P. Hummel,[6] B. V. Jacak,[10] R. Jayanti,[9] K. Kaimi,[5,¶] M. Kaneta,[5,‖] T. Kohama,[5] M. L. Kopytine,[10,**] M. Leltchouk,[3] A. Ljubicic, Jr.,[7] B. Lörstad,[11] N. Maeda,[5,††] L. Martin,[4] A. Medvedev,[3] M. Murray,[8] H. Ohnishi,[5,‡] G. Paic,[6,‡‡] S. U. Pandey,[9] F. Piuz,[6] J. Pluta,[5,§§] V. Polychronakos,[12] M. Potekhin,[3] G. Poulard,[6] D. Reichhold,[9] A. Sakaguchi,[5,‖‖] J. Schmidt-Sørensen,[11] J. Simon-Gillo,[2] W. Sondheim,[2] T. Sugitate,[5] J. P. Sullivan,[2] Y. Sumi,[5] W. J. Willis,[3] K. L. Wolf,[8,¶] N. Xu,[2,‖] and D. S. Zachary[9]

(NA44 Collaboration)

[1]*Niels Bohr Institute, DK-2100 Copenhagen, Denmark*
[2]*Los Alamos National Laboratory, Los Alamos, New Mexico 87545*
[3]*Columbia University, New York, New York 10027*
[4]*Nuclear Physics Laboratory of Nantes, F-44072 Nantes, France*
[5]*Hiroshima University, Higashi-Hiroshima 739, Japan*
[6]*CERN, CH-1211 Geneva 23, Switzerland*
[7]*Rudjer Boscovic Institute, Zagreb, Croatia*
[8]*Texas A&M University, College Station, Texas 77843*
[9]*The Ohio State University, Columbus, Ohio 43210*
[10]*SUNY at Stony Brook, Stony Brook, New York 11794*
[11]*University of Lund, S-22362 Lund, Sweden*
[12]*Brookhaven National Laboratory, Upton, New York 11973*

(Received 10 July 2001; published 4 April 2002)

NA44 uses a 512-channel Si pad array covering $1.5<\eta<3.3$ to study charged hadron production in 158*A* GeV Pb+Pb collisions at the CERN SPS. We apply a multiresolution analysis, based on a discrete wavelet transformation, to probe the texture of particle distributions event by event, allowing a simultaneous localization of features in space and scale. Scanning a broad range of multiplicities, we search for signals of clustering and of critical behavior in the power spectra of local density fluctuations. The data are compared with detailed simulations of detector response, using heavy-ion event generators, and with a reference sample created via event mixing. An upper limit is set on the probability and magnitude of dynamical fluctuations.

DOI: 10.1103/PhysRevC.65.044903 PACS number(s): 25.75.−q

I. INTRODUCTION

The main experimental challenge in relativistic heavy-ion collisions is to find evidence of the expected QCD phase transition at high temperature. Deconfinement and chiral symmetry restoration are expected to take place during the hot, strongly interacting stage early in the collision. As a phase transition in such collisions is inherently a multiparticle phenomenon, multiparticle observables, defined on an event-by-event basis, are of great interest. Recently published event-by-event analyses of the 158-GeV/nucleon Pb+Pb data either analyzed a small number of events [1] in great detail, or analyzed properties of a large ensemble of events using a single observable (p_T) to compare different ensemble averages [2]. In the first case, the accumulation of feature information from large data sets remains an open issue. In the second case, an ensemble average on a set of *post-freeze-out* events is not representative of the *pre-freeze-out* history of those events, due to the dramatic nonstationarity of the open system, with a consequent lack of ergodicity. Violations of ergodicity generally occur in the course of phase transitions [3].

We concentrate on *texture*, or *local fluctuation*, observables, analyzing single events independently to determine the scale composition of fluctuations. In the following, we may omit the term ''local,'' but we will always talk about fluctuations in the particle density from one point to another within a single event, i.e., in a *local* sense, as opposed to fluctuations of *global* quantities from one event to another.

*Now at KEK – High Energy Accelerator Research Organization, 1-1 Oho, Tsukuba, Ibaraki 305, Japan.
†Now at University of New Mexico, Albuquerque, New Mexico 87131.
‡Now at Brookhaven National Laboratory, Upton, New York 11973.
§Now at Los Alamos National Laboratory, Los Alamos, New Mexico 87545.
‖Now at Lawrence Berkeley National Laboratory, Berkeley, California 94720.
¶Deceased.
**On an unpaid leave from P. N. Lebedev Physical Institute, Russian Academy of Sciences.
††Now at Florida State University, Tallahassee, Florida 32306.
‡‡Affiliated with Ohio State University, Columbus, Ohio 43210.
§§Institute of Physics, Warsaw University of Technology, Koszykowa 75, PL-00-662 Warsaw, Poland.
‖‖Now at Osaka University, Toyon aka, Osaka 560-0043, Japan.

In 1985, Van Hove formulated a model of quark-gluon plasma hadronization [4] with a first-order phase transition. A longitudinal expansion of the colliding system, with particle formation via string or color flux tube breaking, can result in plasma droplets as large as a few fm across. The droplets hadronize by *deflagration* [5]. This is expected to result in dN/dy distributions with bumps or spikes on top of an otherwise smooth structure. Other models [6] also predicted bubbles of one phase embedded in the other.

In the absence of a direct, event-by-event observable-based test of these predictions, the picture was further developed [7,8] in order to connect it with traditional observables such as the m_T slope parameter T and the baryon and strangeness chemical potentials: the hadron ''temperatures'' T in the SPS data are higher than lattice QCD predictions for a phase-transition temperature. Using a first-order phase-transition hydrodynamical model with a sharp front between the phases, Bilic and co-workers [7,8] concluded that quark-gluon plasma (QGP) *supercooling* and hadron gas *superheating* are consequences of the continuity equations and of the requirement that the entropy be increased in the transition. In the case of bubbles in the QGP phase, the plasma deflagrates; otherwise it detonates. A direct measurement of the hadron texture at freeze-out, if it detects the presence of droplets or bubbles, could provide an argument in favor of the first-order phase transition.

The order of the confinement phase transition is still under debate. It is a fluctuation-driven first-order transition [9,10] in SU(3) with three massless quarks, but second order in the case of finite mass [11] or infinitely massive [9,10] strange quarks. A tricritical point may exist, separating the first-order transition from a second-order transition with the same critical exponents as the three-dimensional (3D) Ising model [9]. For a second-order phase transition, local fluctuations of isospin or enhanced correlation lengths may be observable [12,13]. Large-scale correlations formed early in the collision are more likely to survive diffusion in the later stages. Small-scale fluctuations, conversely, are more easily washed out by diffusion due to secondary scattering among the hadrons [14]. Consequently, an analysis method which can identify fluctuations on any scale is desirable. In this paper, we utilize a discrete wavelet transformation, which has this property.

A wavelet is a function zero everywhere except for a well-localized spot. For a pad detector, the discrete positions of the spots correspond naturally to the pad positions, and the possible scales are multiples of the pad sizes. The scale is an analog of the Fourier frequency. Location has no analog in the Fourier transform, and it provides an additional degree of analytical power, which explains much of the success that wavelets met in the fields of data processing and pattern recognition. (Examples of Fourier-based analyses of large-scale azimuthal texture in the field of relativistic heavy-ion, collisions also exist [15,16]; this is how the elliptic flow at ultrarelativistic energies was measured.) The binning of the charged particle density inherent in measurements with a segmented detector such as a Si pad detector makes the Haar wavelet a natural choice of analyzing function; a Haar wavelet is a step function with given width, oscillating around zero with a single period.

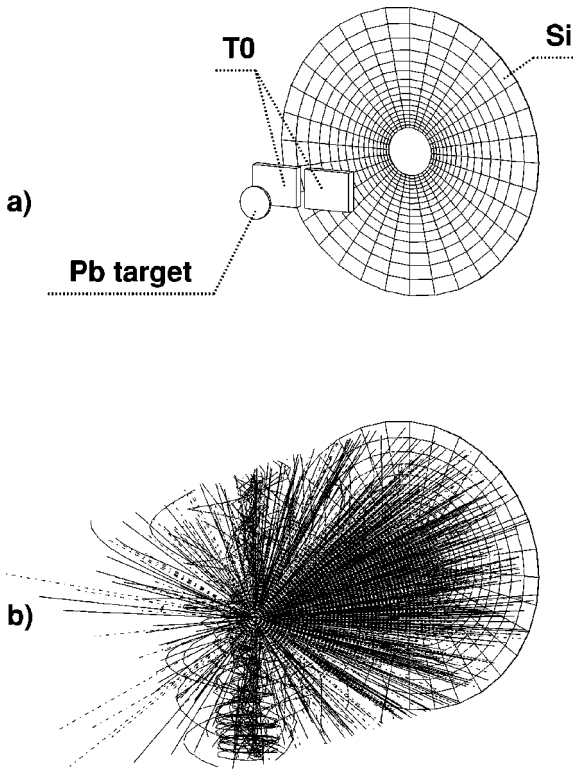

FIG. 1. (a) The experimental setup: the target, the Si pad array, and the $T0$ scintillation counter. See the text for a description of the detectors. (b) The setup exposed to an RQMD event (GEANT simulation). The magnetic field is on.

The discrete wavelet transformation (DWT) [17] quantifies contributions of different ϕ and η scales to the event texture. We use a DWT to test for possible large-scale enhancement, as a function of the collision centrality. We report the DWT power spectrum in pseudorapidity η and azimuthal angle ϕ, for different charged particle multiplicities. We use mixed events to remove trivial fluctuations and background effects.

II. EXPERIMENTAL SETUP

The experimental setup [18] is shown in Fig. 1. The NA44 Si pad array, installed 10 cm downstream from the target, in the magnetic field of the first dipole, measured ionization energy loss of charged particles in its 512 300-μm-thick Si pads. The plastic scintillator $T0$ (two rectangles seen in Fig. 1) was used for a centrality trigger. The SPS beam was collimated to a 1×2-mm^2 profile. $T0$ covered $1.4\leqslant\eta\leqslant3.7$ for an η-dependent fraction of azimuthal angle, $0.22\leqslant\Delta\phi/2\pi\leqslant0.84$, respectively. The silicon detector had an inner radius of 7.2 mm and an outer radius of 43 mm, covering $1.5\leqslant\eta\leqslant3.3$. The detector was split *radially* into 16 rings of equal η coverage. Each ring was further divided *azimuthally* into 32 sectors of equal angular coverage to form pads. The pads were read out by AMPLEX [19] chips, one chip per sector. δ electrons, produced by the Pb beam tra-

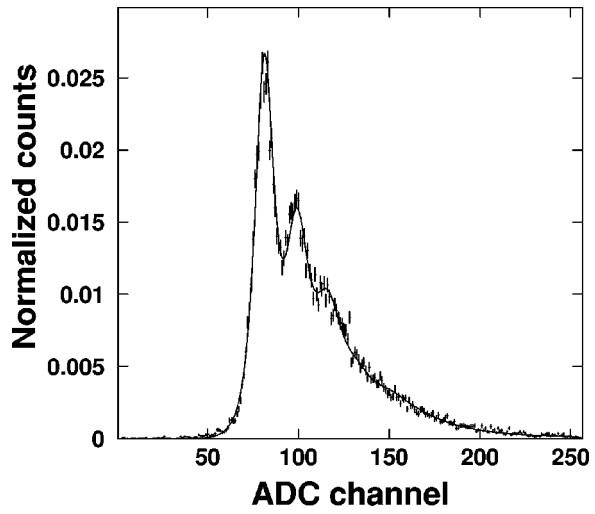

FIG. 2. Digitized amplitude distribution from channel 1 of the Si pad array. The smooth curve shows a minimum χ^2 Landau fit performed in the course of the amplitude calibration. The pedestal and the single and double hit peaks are distinguishable.

versing the target, were swept away to one side by the dipole magnetic field ($\leqslant 1.6$ T). Only the δ-electron-free side was used in this analysis. Only four of the remaining 256 channels were inoperative.

An amplitude distribution from a typical channel, observed in the physics run and digitized with a 256 channel analog-to-digital converter (ADC) is shown on Fig. 2. Channel pedestals had, on the average, a full width at half maximum of 0.48 (dE) of one minimum ionizing potential (MIP). In the texture analysis, every event was represented by a 2D array of the calibrated digitized amplitudes of the channels (an *amplitude array*). Empty target runs were used to measure the background, and cross-talk in the detector was evaluated off-line.

III. ANALYSIS TECHNIQUE

A. Detector calibration

The NA44 spectrometer information was not used in this analysis, which focused on the Si pad array data. ADC pedestals were fitted channel by channel with a realistic functional shape, determined from low multiplicity events in a minimum bias triggered run. The amplitude calibration of the Si detector was carried out channel by channel, by fitting the amplitude distribution with a sum of single, double, triple, etc. (up to septuple) minimum ionizing particle Landau distributions [20] with variable weights. The Landau distributions were numerically convoluted with the pedestal shape to account for noise in the fit. A typical fit from a single channel is shown in Fig. 2. Parameters of the fit were used to simulate noise in a GEANT-based [41] detector response Monte Carlo code.

An offset of the event vertex with respect to the detector's symmetry axis results in a nontrivial functional dependence between the actual η and ϕ, and the η' and ϕ' presumed based on the "ideal" geometry: $\eta=\eta(\eta',\phi'),\phi=\phi(\eta',\phi')$. This makes the observable multiplicity distribution $d^2N/d\phi' d\eta'$ (in the presumed coordinates) differ from a simple function of η':

$$\frac{d^2N}{d\phi' d\eta'} \neq \frac{1}{2\pi}\frac{dN}{d\eta'}. \tag{1}$$

In the true coordinates η and ϕ, inequality (1) becomes an equality. However, the detector's acceptance area in the true coordinates becomes distorted. In the following we will refer to this as a "Jacobian effect." The Jacobian effect, obviously, contributes to the event textures, especially on a large scale, and needs to be evaluated and corrected for.

From Eq. (1), the criterion of the true coordinate basis (η,ϕ) emerges naturally: it is the basis which makes the observable $d^2N/d\phi d\eta$ independent of ϕ. The minimization problem was solved numerically with MINUIT [21], and the resulting offsets are within the tolerance of the detector or beam position. Cross-talk between the electronics channels is a detector-related correlation phenomenon, and introduces a "texture" effect of its own. Both global cross-talk in the AMPLEX read-out chip [19] and read-out board cross-talk are expected. In our detector with 512 channels, there are $512\times(512-1)/2=130\,816$ two-channel pairs (unordered), all of which were subjected to covariance analysis off-line. To magnify the nontrivial instrumental contribution to the covariance matrix elements, we analyzed covariances not between the amplitudes A_i of channels i themselves, but between

$$a_i=A_i-\frac{\sum_{\text{half-ring of } i} A_k}{\sum_{\text{half-ring of } i} 1}=A_i-\frac{1}{16}\sum_{\text{half-ring of } i} A_k. \tag{2}$$

Otherwise, the dominant contributor to the $\mathrm{cov}(A_i,A_j)$ is the trivial variation of the event's common multiplicity [22]. Using this method, we concluded that the effective cross-talk coupling was non-negligible only for neighboring channels within the same chip; it was found to be 8.5%. As a remedy, a chip-wise (i.e., sector-wise) event mixing technique, including cross-talk in the reference sample, was used to construct a reference event sample.

The double-differential multiplicity data (Fig. 3) illustrate the quality of the detector operation, calibrations, geometrical alignment, and Jacobian correction. The data set is composed of two pieces, obtained by switching the magnetic-field polarity: a negative polarity run is used for sectors 9–24 (range of $\pi/2<\phi<3\pi/2$); a positive polarity run is used for sectors 1–8 and 25–32 (ranges of $0<\phi<\pi/2$ and $3\pi/2<\phi<2\pi$). The reason to disregard one side of the detector is the additional occupancy due to δ electrons, as explained in Sec. II. Figure 3 demonstrates the quality of alignment as well, since η and ϕ along the horizontal axes are the aligned coordinates. Any geometrical offset of the detector makes the acceptances of different pads nonequal and dependent on the pad position. The acceptance of each pad has been calculated in the aligned coordinates, and the $d^2N/d\phi d\eta$ uses the actual acceptances $d\phi\, d\zeta$. The shape of the ϕ dependence of

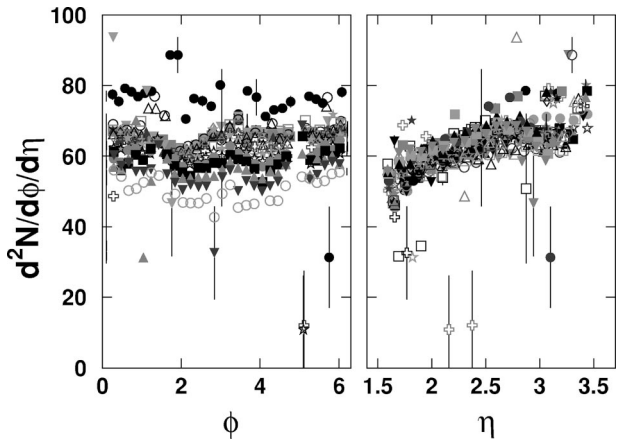

FIG. 3. Double-differential multiplicity distributions of charged particles plotted as a function of the azimuthal angle ϕ (with different symbols representing different rings) and of the pseudorapidity η (with different symbols representing different sectors). ϕ and η are in *aligned* coordinates.

$d^2N/d\phi d\eta$ (left panel of Fig. 3) is flat, as it should be for an event ensemble with no reaction plane selection. The η dependence (right panel of Fig. 3) shows an increasing multiplicity toward midrapidity, as expected. As can be seen from Fig. 3, the detector's acceptance is asymmetric around midrapidity. A correction for the cross-talk has been applied.

B. Discrete wavelet transformation (DWT)

Discrete wavelets are a set of functions, each having a proper width or scale, and a proper location so that the function differs from 0 only within that width and around that location. The set of possible scales and locations is discrete. The DWT formalizes the two-dimensional particle distribution in each Pb+Pb collision in pseudorapidity η and azimuthal angle ϕ by performing an image analysis—transforming the event into a set of functions orthogonal with respect to scale and location in the (η,ϕ) space. We accumulate texture information by averaging the power spectra of many events.

The simplest DWT basis is the Haar wavelet, built upon the *scaling function* [23] $g(x)=1$ for $0\leqslant x<1$, and 0 otherwise. The function

$$f(x)=\begin{cases}+1, & 0\leqslant x<\frac{1}{2}\\ -1, & \frac{1}{2}\leqslant x<1\\ 0, & \text{otherwise}\end{cases} \tag{3}$$

is the wavelet function [24].

If the interaction vertex lies on the detector's symmetry axis, every pad's acceptance is a rectangle in the (ϕ,η) space. Then the Haar basis is the natural choice, as its scaling function in two dimensions $G(\phi,\eta)=g(\phi)g(\eta)$ is just a pad's acceptance (modulo units). We set up a two dimensional wavelet basis:

$$F^{\lambda}_{m,i,j}(\phi,\eta)=2^m F^{\lambda}(2^m\phi-i,2^m\eta-j). \tag{4}$$

The scaling function in two dimensions is $G(\phi,\eta)=g(\phi)g(\eta)$. As in Eq. (4), we construct $G_{m,i,j}(\phi,\eta)$ where m is the integer scale fineness index, and i and j index the positions of bin centers in ϕ and η ($1\leqslant m\leqslant 4$ and $1\leqslant i,j\leqslant 16$ because we use $16=2^4$ rings and 16 sectors). Different values of λ (denoted as ϕ, η, and $\phi\eta$) distinguish, respectively, functions with azimuthal, pseudorapidity, and diagonal texture sensitivity:

$$F^{\phi}=f(\phi)g(\eta),\quad F^{\eta}=g(\phi)f(\eta),\quad F^{\phi\eta}=f(\phi)f(\eta). \tag{5}$$

Then $F^{\lambda}_{m,i,j}$, with integers m, i, and j, are known [17] to form an orthonormal basis in the space of all *measurable functions* defined on the continuum of real numbers $L^2(\mathbb{R})$. Figure 4 shows the wavelet basis functions F in two dimensions. At first glance it might seem surprising that, unlike the 1D case, both f and g enter the wavelet basis in two dimensions. Figure 4 clarifies this: in order to fully encode an arbitrary shape of a measurable 2D function, one considers it as an addition of a change along ϕ [$f(\phi)g(\eta)$, panel (b)], a change along η [$g(\phi)f(\eta)$, panel (c)], and a saddle-point pattern [$f(\phi)f(\eta)$, panel (a)], added with appropriate weight (positive, negative, or zero), for a variety of scales. The finest scale available is determined by the detector segmentation, while coarser scales correspond to successively rebinning the track distribution. The analysis is best visualized by considering the scaling function $G_{m,i,j}(\phi,\eta)$ as binning the track distribution $\rho(\phi,\eta)$ in bins i,j of fineness m, while the set of wavelet functions $F^{\lambda}_{m,i,j}(\phi,\eta)$ (or, to be exact, the wavelet

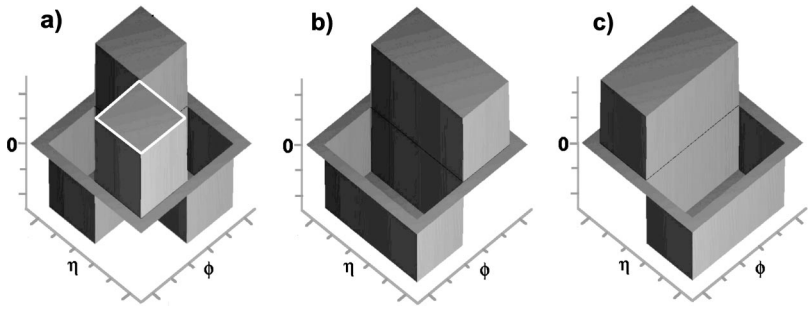

FIG. 4. Haar wavelet basis in two dimensions. The three modes of directional sensitivity are (a) diagonal, (b) azimuthal, and (c) pseudorapidity. For the finest scale used, the acceptance of a Si pad would correspond to the white rectangle drawn "on top" of the function in panel (a). Every subsequent coarser scale is obtained by expanding the functions of the previous scale by a factor of 2 in both dimensions.

expansion coefficients $\langle \rho, F^{\lambda}_{m,i,j} \rangle$) gives the difference distribution between the data binned with given coarseness and that with binning one step finer.

While the DWT analyzes the object (an image, a sequence of data points, a data array) by transforming it, the *full* information content inherent in the object is preserved in the transformation.

We adopt the existing [25] 1D DWT power spectrum analysis technique, and expand it to two dimensions. The track density in an individual event is $\rho(\phi, \eta)$ and its *local* fluctuation in a given event is $\sigma^2 \equiv \langle \rho - \overline{\rho}, \rho - \overline{\rho} \rangle$, where $\overline{\rho}$ is the average ρ (over the acceptance) in the given event [26].

Using the completeness of the basis, we expand

$$\rho - \overline{\rho} = \langle \rho, F^{\lambda}_{m,i,j} \rangle F^{\lambda}_{m,i,j} - \langle \overline{\rho}, F^{\lambda}_{m,i,j} \rangle F^{\lambda}_{m,i,j}. \tag{6}$$

Note that $\overline{\rho}$, being constant within the detector's rectangular acceptance, is orthogonal to any $F^{\lambda}_{m,i,j}$ with $m \geqslant 1$. Due to the orthonormality condition $\langle F^{\lambda}_{m,i,j}, F^{\lambda'}_{m',i',j'} \rangle = \delta_{\lambda,\lambda'} \delta_{m,m'} \delta_{i,i'} \delta_{j,j'}$, the $\rho - \overline{\rho}$ components for different scales do not form cross-terms in the σ^2 sum, and the sum contains no cross-terms between ρ and $\overline{\rho}$ for the four observable scales. Instead of a $\langle \rho, G_{m=5,i,j} \rangle$ set, the Si detector energy amplitude array—its closest experimentally achievable approximation—is used as the DWT input. We used the WAILI [27] software library to obtain the wavelet decompositions.

The Fourier power spectrum of a random white-noise field is known to be independent of frequency [29]. We are looking for dynamical textures in the data, and therefore would like to treat the random white noise case as a ''trivial'' one to compare with. Therefore, it is interesting to reformulate this property for wavelets, where scale plays the same role as frequency in a Fourier analysis.

To do this we link scales with frequencies, or in other words, we must understand the frequency spectra of the wavelets. The Fourier images of 1D wavelet functions occupy a set of wave numbers whose characteristic broadness grows with scale fineness m as 2^m; 2^{2m} should be used in the 2D case. Discrete wavelets of higher orders have better frequency localizations than the Haar wavelets. Despite this advantage, we use Haar wavelets because only Haar wavelets allow one to say that the act of data taking with the (binned) detector constitutes the first stage of the wavelet transformation.

In two dimensions, we find it most informative to present the three modes of a power spectrum with different directions of sensitivity $P^{\phi\eta}(m)$, $P^{\phi}(m)$, and $P^{\eta}(m)$ separately. We define the *power spectrum* as

$$P^{\lambda}(m) = \frac{1}{2^{2m}} \sum_{i,j} \langle \rho, F^{\lambda}_{m,i,j} \rangle^2, \tag{7}$$

where the denominator gives the meaning of spectral *density* to the observable. So defined, the $P^{\lambda}(m)$ of a random white-noise field is independent of m.

In order to illustrate the sensitivity of the wavelet transformation to texture features of the different scales, we have applied the wavelet transform to three test patterns, shown in Fig. 5. All patterns are 16×16 pixel matrices. The left-hand side shows the test pattern, and the right shows the power spectrum resulting from the wavelet transform. Pattern (a), a checkerboard, has structure only on the finest scale and all power components of scales coarser than 4 are zero. Pattern (b) has exactly the opposite scale composition: the slow gradation between black and white corresponds to a structure on the coarsest scale, as seen in the accompanying power spectrum. The smoothness of the gradient means that neighbor-to-neighbor changes do not add much to the pattern once the overall trend (the large scale feature) is taken into account.

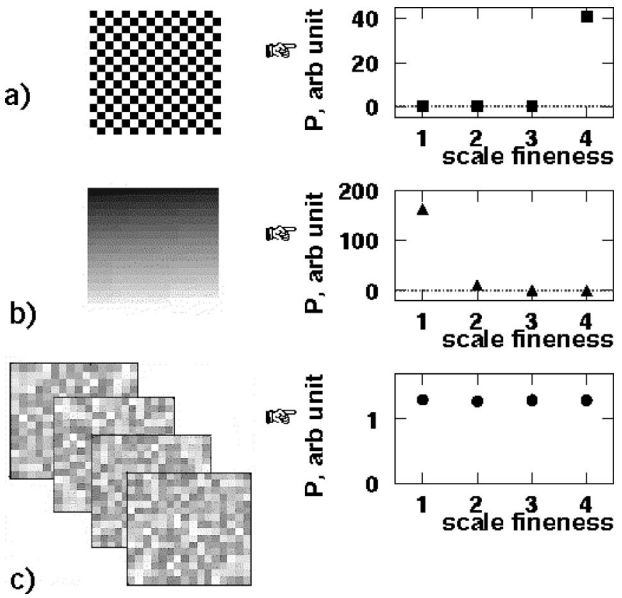

FIG. 5. Understanding the analyzing potency of the DWT power spectra: (a) for a checkerboard pattern, (b) for a smooth gradient pattern, and (c) for a sample of a thousand random white noise images—in this case the *average* power spectrum is shown.

These two examples illustrate the property of scale localization, made possible by virtue of the scale orthogonality of the basis. Patterns encountered in multiple hadron production involve a variety of scales, and yet they are more likely to be of type (b) rather than (a). An important conclusion follows immediately: in this type of measurement, large acceptance, like the one used in this analysis, rather than fine segmentation, is the way to accomplish sensitivity.

Case (c) shows patterns that arise from white noise. They produce signals in the power spectrum independent of scale, as expected. In the first approximation, the white noise example provides a base-line case for comparisons in a search for nontrivial effects.

Figure 6 shows the power spectra measured in Pb+Pb for one multiplicity range. The unit on the vertical scale $[\sigma^2/\langle dE_{MIP} \rangle^2]$ is chosen so that the power of fluctuations, whose variance σ^2 is equal to the squared mean energy loss by a minimum ionizing particle traversing the detector, is the unit. The first striking feature is that the power spectra of physical events are indeed enhanced on the coarse scale. The task of the analysis is to quantify and, as much as possible, eliminate ''trivial'' and experiment-specific reasons for this enhancement.

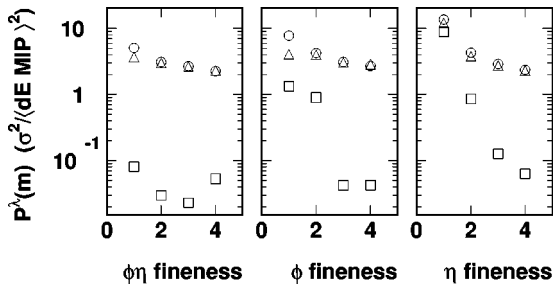

FIG. 6. Power spectra of 7×10^3 events in the multiplicity bin $326<dN/d\eta<398$ (between $\approx$6% and 10% centrality). ○, true events; △, mixed events; □, the average event.

C. Identification and control of systematic errors

The average event, formed by summing amplitude images of the measured events in a given multiplicity bin, and dividing by the number of events, has a much reduced texture as statistical fluctuations cancel (shown as □ in Fig. 6). Average events retain the texture associated with the shape of $d^2N/d\phi d\eta$, with the dead channels and the finite beam geometrical cross section (though this is only partially visible in the average event, due to the fact that event averaging is done without attempting to select events according to the vertex position). $P^{\lambda}(m)$ is proportional to the variance, or squared fluctuation σ^2. Therefore, for Poissonian statistics of hits in a pad, the event averaging over M events should decrease $P^{\lambda}(m)$ by a factor of M. The average event whose power spectrum is shown on Fig. 6 is formed by adding 7×10^3 events; however, its $P^{\lambda}(m)$ is down less than 7×10^3 compared to that of the single events. This demonstrates that the average event's texture is not due to statistical fluctuations, but, rather is, *predominantly* due to the systematic uncertainties listed. Consequently, we can use the average event's $P^{\lambda}(m)$ to estimate the magnitude of the static texture-related systematics. As seen from Fig. 6, the systematics are far below the $P^{\lambda}(m)$ of single events (true or mixed), with the exception of pseudorapidity, where the nonconstancy of $dN/d\eta$ over the detector's acceptance is visible.

The way to get rid of the ''trivial'' or static texture is to use mixed events, taking different channels from different events. The mixed events preserve the texture associated with the detector position offset, the inherent $dN/d\eta$ shape, and the dead channels. This is a *static* texture, as it produces the same pattern event after event while we are searching for evidence of dynamic texture. We reduce sources of the static texture in the power spectra by empty target subtraction and by subtraction of mixed events power spectra, thus obtaining the *dynamic texture* $P^{\lambda}(m)_{true}-P^{\lambda}(m)_{mix}$. In order to reproduce the electronic cross-talk effects in the mixed event sample, the mixing is done sector-wise, i.e., the sectors constitute the subevents subjected to the event number scrambling.

We continue with a brief summary of the systematic errors in the measurements of the DWT dynamic texture observable $P_{true}-P_{mix}$. The static texture and dynamic background texture present the largest problem in the search for the phase transition-related dynamic texture via the power spectra of local fluctuations. The method of solving the problem is a comparison with the reference sample created by event mixing. Thus the $P_{true}-P_{mix}$ observable was created. For comparison with models, a Monte Carlo simulation of the Si detector is used. It includes the known static texture effects and undergoes the same procedure to remove the effects. The ''irreducible remainder'' is the residual effect which may (1) survive the elimination procedure, and (2) emerge *as a difference* between the data, subjected to the elimination procedure, and the MC analyzed in the same manner.

Table I lists the sources of static texture and summarizes the methods of their treatment. We group the *background texture* sources according to similarity of manifestation and treatment, into (i) statistical fluctuations, (ii) static texture, and (iii) background dynamic texture.

The statistical fluctuation is the most trivial item in this list. Both event mixing (provided that mixing is done within the proper multiplicity class) and a Monte Carlo (MC) comparison solve this problem. The statistical fluctuations do not result in irreducible systematic errors.

The static texture group includes (i) the geometrical offset of the detector with respect to the beam's ''center of gravity'' in the vertical plane, (ii) dead pads, and (iii) the $dN/d\eta$ shape: a genuine large scale multiparticle correlation sensitive to the physics of the early stage of the collision.

The cleanliness of the static texture elimination via event mixing has been checked by simulating the contributing effects separately. First, we ran the detector response simulation on MC-generated events *without* an offset of the beam with respect to the detector and with a beam of zero thickness, it was ascertained that the remaining dynamic texture is very small compared with the systematic errors due to the background Si hits and the beam geometrical cross section, for all scales and all directional modes λ. Due to the finite size of the multiplicity bin, the mixed events consist of subevents coming from events of different total multiplicity. With the sector-wise mixing, this causes an additional sector-to-sector variation of amplitude in the mixed events, thus resulting in an enhancement of P^{ϕ}_{mix} primarily on the finest scale, with respect to P^{ϕ}_{true}. In Fig. 7, this effect can be seen as the $P^{\phi}_{true}-P^{\phi}_{mix}$ values progressively grow negative with multiplicity in the finest scale plot. However, as can be seen on the same figure, the effect is small compared with the total systematic error bars shown as boxes.

The background dynamic texture group includes (i) elliptic and directed flow, (ii) finiteness of the beam cross section, (iii) background hits in the Si, and (iv) the channel-to-channel cross-talk.

Elliptic and directed flows, observed at SPS [16], are large-scale dynamic texture phenomena of primarily azimuthal (elliptic) and diagonal (directed flow) modes. Because both the reaction plane and direction angle vary event by event, the respective dynamic textures cannot be subtracted by event mixing, unless the events are classified according to their reaction plane orientation and the direction angle, with mixing and $P_{true}-P_{mix}$ subtraction done within those classes. Neither the reaction plane nor direction angle was reconstructed in the present analysis, and $P_{true}-P_{mix}$

TABLE I. Sources of background texture (dynamic and static) and their treatment. The irreducible remainder estimate is quoted for diagonal texture correlation in the $326<dN/d\eta<398$ bin, and is expressed in the units of $\sigma^2/\langle dE_{MIP}\rangle^2$; see text for information on how it was obtained.

Source	Correction event mixing: subtract empty target	subtract mixed events	preserve sectors	do MC	Irreducible remainder estimate $\sigma^2/\langle dE_{MIP}\rangle^2$
stat. fluctuations	N/A	yes	N/A	yes	0
$dN/d\eta$ shape, offset, dead pads	N/A	yes	OK	yes	0
finite beam Xsection 1×2 mm	N/A	N/A	N/A	yes	0.14
background hits	yes	yes	yes	can't	$>0.070,<0.37$
channel Xtalk 8.5% for neighbors	N/A	yes	yes	can't	$>0.070,<0.37$

(especially that of the azimuthal and diagonal modes on the coarse scale) retains the elliptic and directed flow contribution. The effects of flow on dynamic texture observables are smaller than other texture effects, so they cannot be singled out and quantified in this analysis.

The finite beam cross-section effect belongs to this group, despite the fact that a very similar effect of the geometrical detector or beam offset has been classified as static texture. An effect must survive mixing with its strength unaltered in order to be fully subtracted via event mixing. Preserving the effect of random variations in the Pb+Pb vertex on the power spectra in the mixed events requires a classification of events according to the vertex position, and mixing only within such classes. This requires a knowledge of the vertex for each event, which is not available in this experiment. Therefore, a MC simulation of the beam profile remains the only way to quantify the false texture arising from vertex variations. MC studies with event generators showed that the beam spatial extent and the resulting vertex variation is the source of the growth of the coarse scale *azimuthal* texture correlation with multiplicity (see Fig. 7). The uncertainty in our knowledge of the beam's geometrical cross-section must be propagated into a systematic error on $P_{true}-P_{mix}$.

The other two effects in this group are difficult to separate and simulate, and the error estimate reflects the combined effect. The systematic errors were evaluated by removing the Pb target and switching the magnetic-field polarity to expose the given side of the detector to δ electrons (from the air and $T0$), while minimizing nuclear interactions. This gives an "analog" generator of uncorrelated noise. All correlations [i.e., deviations of $P^{\lambda}(m)_{true}$ from $P^{\lambda}(m)_{mix}$] in this noise generator are treated as systematic uncertainties. Thus this component of the systematic error receives a sign, and the systematic errors are asymmetric. The effect of increasing the texture correlation (for diagonal and azimuthal modes) with multiplicity, on a coarse scale, attributed to the geometrical offset of the detector with respect to the beam (the leading one in the static group), is present in the switched polarity empty target runs as well. For this reason, it was impossible to disentangle the background dynamic contribution on the coarsest scale. In Table I, the "irreducible remainder estimate" for the diagonal, coarse scale is bracketed with two numbers, which form the lower and upper estimates. The lower estimate is obtained by taking the scale one unit finer and quoting its number. This, indeed, sets the lower limit because the deviations of $P^{\lambda}(m)_{true}$ from $P^{\lambda}(m)_{mix}$ generally grow with scale coarseness. The upper limit is set by ascribing the *entire* texture correlation, observed in the δ-electron data, to the background hits and channel crosstalk, and ignoring the fact that significant portion of it must be due to the vertex fluctuation (finite beam profile). This upper limit is likely to be a gross overestimation, and in Fig. 7 we show systematic errors, obtained by adding in quadrature the finite beam error with the background hit error.

IV. RESULTS

Figure 7 presents a comparison of the DWT dynamic texture in the measured and relativistic quantum molecular dynamics (RQMD) simulated [30] Pb+Pb collision events. The three directional sensitivity modes (diagonal $\phi\eta$, azimuthal ϕ, and pseudorapidity η) have four scales each, so that there are 12 sets of points in the DWT dynamic texture as a function of the charged multiplicity $dN_{ch}/d\eta$ bin. The systematic errors on the points (shown by vertical bars) have been evaluated following the procedure described in detail in Sec. III.

Figure 6 demonstrates that the major fraction of the observed texture also exists in mixed events. A detailed account

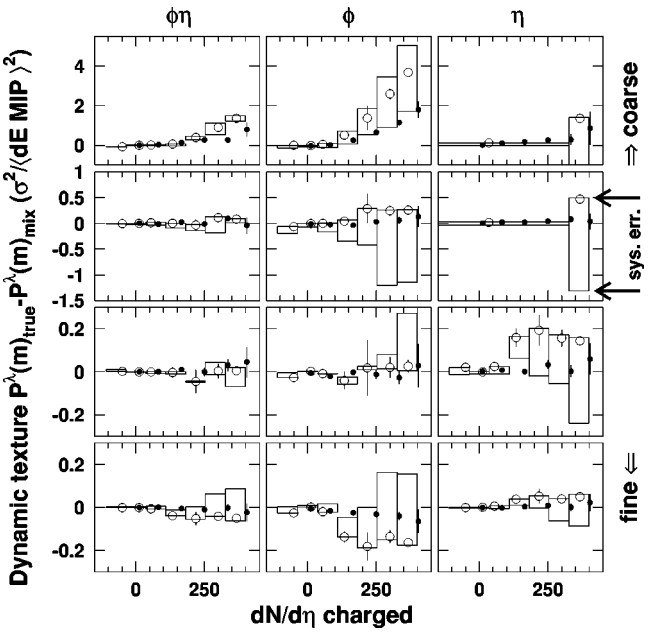

FIG. 7. Multiplicity dependence of the texture correlation. ○, the NA44 data; ●, RQMD. The boxes show the systematic errors vertically and the boundaries of the multiplicity bins horizontally; the statistical errors are indicated by the vertical bars on the points. The rows correspond to the scale fineness *m*, the columns to the directional mode λ (which can be diagonal $\phi\eta$, azimuthal ϕ, and pseudorapidity η).

of the causes was discussed in Sec. III, including known physics as well as instrumental effects. It is therefore clear that the observable most directly related to the dynamical correlations and fluctuations is not $P^\lambda(m)$ but $P^\lambda(m)_{true} - P^\lambda(m)_{mix}$. This quantity, normalized to the rms fluctuation of $P^\lambda(m)_{mix}$, can be used to characterize the relative strength of local fluctuations in an event. The distribution for different λ (or directions) is plotted in Fig. 8 in an integral way, i.e., as an $\alpha(x)$ graph where, for every x, α is the fraction of the distribution above x:

$$\alpha(x) = \int_x^\infty \frac{dN}{d\xi} d\xi \Big/ \int_{-\infty}^{+\infty} \frac{dN}{d\xi} d\xi, \tag{8}$$

where ξ denotes the fluctuation strength,

$$\xi = \frac{P^\lambda(1)_{true} - P^\lambda(1)_{mix}}{RMS[P^\lambda(1)_{mix}]}, \tag{9}$$

and $dN/d\xi$ is the statistical distribution of ξ, obtained from the experimentally known distributions of $P^\lambda(1)_{true}$ and $P^\lambda(1)_{mix}$. Expression (9) is constructed to be sensitive to the difference between $P^\lambda(1)_{true}$ and $P^\lambda(1)_{mix}$, while minimizing detector specifics to enable comparison between different experiments in future. The latter is accomplished by normalizing to RMS_{mix}. This normalization also eliminates the trivial multiplicity dependence of the observable.

The fluctuation strength observable provides a limit on the frequency and strength of the fluctuations and expresses the result in a model-independent way. The *confidence level* with

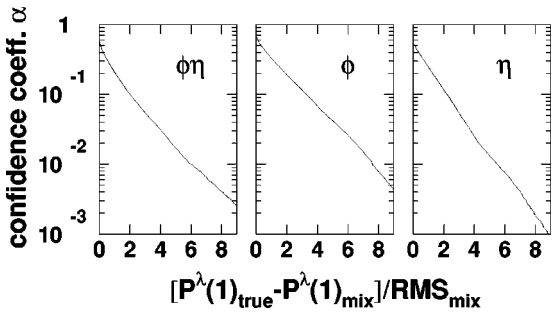

FIG. 8. Confidence coefficient as a function of the fluctuation strength. RMS_{mix} denotes $\sqrt{\langle P^\lambda(1)^2_{mix} - \langle P^\lambda(1)_{mix}\rangle^2\rangle}$. The multiplicity bin is $326 < dN/d\eta < 398$ (6–10 % centrality), as in Fig. 6.

which local fluctuations of a given strength [expressed through the event-by-event observables via Eq. (9)] can be excluded is then $1-\alpha$. Fluctuations greater than $3 \times RMS_{mix}$ are excluded in the azimuthal and pseudorapidity modes with 90% and 95% confidence, respectively. The monotonic fall of the curve is consistent with the absence of abnormal subsamples in the data.

RQMD events were fed into the GEANT detector response simulation and analyzed using the same off-line procedure as used for the experimental data. The detector offset with respect to the beam center of gravity and the beam profile were included in the simulation. In a separate simulation run, the beam profile was identified as the cause of the rise of the azimuthal dynamic texture with the multiplicity on the coarse scale. In our experiment, this purely instrumental effect dominates the azimuthal component of the DWT dynamic texture.

The most apparent conclusion from Fig. 7 is that a large fraction of the texture (seen on Fig. 6) is not dynamic, i.e., not different between true and mixed events. Being monotonic (or absent), the change of the data points with multiplicity does not reveal any evidence of a region of impact parameters or baryochemical potentials with qualitatively different properties, such as those of a critical point neighborhood. The RQMD comparison confirms that particle production via hadronic multiple scattering, following string decays (without critical phenomena or phase transition) can explain the observed results when detector imperfections are taken into account. A more detailed discussion of the implications of these data on various phase transition models will be given in Sec. VI.

V. SENSITIVITY

Interesting physics can manifest itself in the ensemble probability density distributions as well as in the event-by-event (EbyE for short) observables. To illustrate the power of the EbyE observable we used, we should construct final states of charged particles indistinguishable from the point of view of ''traditional,'' or ensemble-wise observables, such as (1) dN/dy distribution, (2) dN/dp_T, $1/mTdN/dm_T$ distributions, etc., and (3) multiplicity distribution, and compare the sensitivity of the above-mentioned observables with that of the EbyE one.

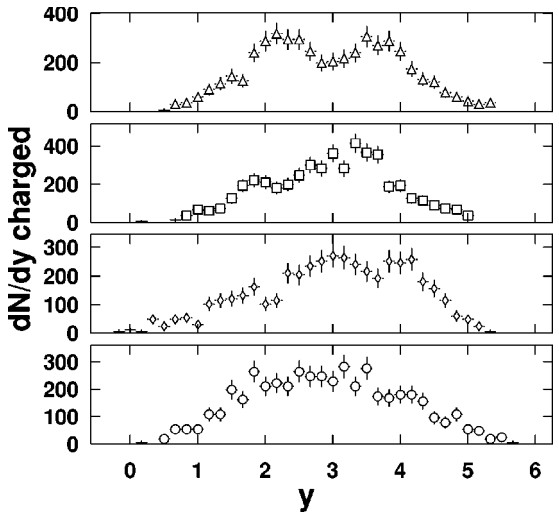

FIG. 9. dN/dy distribution of charged particles in the multifireball event generator in four *individual events* with different number of fireballs: △, two fireballs; □, four fireballs; ◇, eight fireballs; ○, 16 fireballs. One can see how the texture becomes smoother as the number of fireballs increases. We remind the reader that the detector's active area covers π azimuthally and the pseudorapidity from 1.5 to 3.3. In general, acceptance limitations make it more difficult to detect dynamic textures.

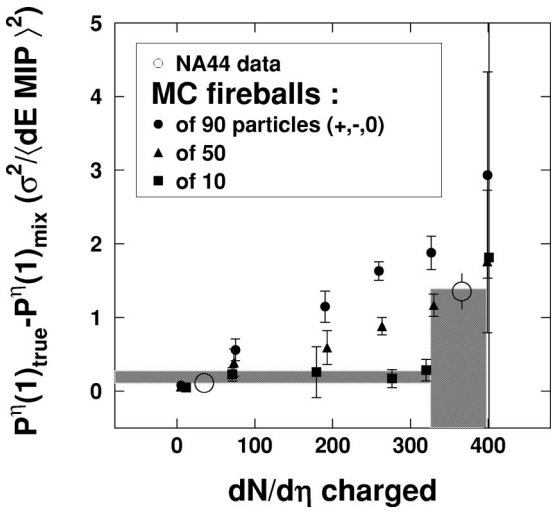

FIG. 10. Coarse scale η texture correlation in the NA44 data, shown by ○ (from the top right plot of Fig. 7), is compared with that from the multifireball event generator for three different fireball sizes. Detector response is simulated. The boxes represent systematic errorbars (see the caption of Fig. 7).

A sensitivity study was performed using a multifireball event generator created specially for this purpose. The generator produces textures of known magnitude by simulating the observed multiplicity as arising from an arbitrary number of fireballs. Correlations among groups of particles arise when the particles come from the same fireball. We do not suggest that the physics of Pb+Pb collisions is properly described by a superposition of fireballs of a fixed size. Rather, we use the fireballs as a way to generate controlled multiparticle correlations.

This picture is inspired by Van Hove's scenario [4] of a first-order phase transition via droplet fragmentation of a QGP fluid. We measure texture in two directions, spanned by polar and azimuthal angles, and are also sensitive to the spatial texture of longitudinal flow. For a boost-invariant expansion [31], two droplets, separated along the longitudinal coordinate, will be separated in y and η. As long as there is a longitudinal expansion, a spatial texture will be manifested as a (pseudo)rapidity texture. In the multifireball event generator, we generate the pseudorapidity texture explicitly, omitting the spatial formulation of the problem. The total p_T of each fireball is 0; its total p_Z is chosen to reproduce the observed dN/dy of charged particles by Lorentz boosting the fireballs along the Z direction, keeping the total $\vec{p}$ of an event at 0 in the rest frame of the colliding nuclei. The fireballs hadronize independently into charged and neutral pions and kaons mixed in a realistic proportion. By varying the number of particles N_p per fireball, one varies the ''grain coarseness'' of the event texture in η.

To illustrate the discussion, Fig. 9 presents examples of dN/dy distributions in four events with different number of fireballs. The dynamic textures seen on the figures are peculiar to these particular events, and are gone after dN/dy of many events are added.

We simulated average fireball multiplicities of 10, 50, 90 (with *RMS* fluctuation of 3), and larger. Figure 10 shows comparison of our data with the simulated pseudorapidity tex- ture. With $\sim 10^4$ events, the detector plus software can differentiate between the cases of 50 and 90 particle fireballs. The signal grows with the charged particle multiplicity and with N_p. Figure 10 provides *quantitative* information on the sensitivity of the texture measurements by relating the expected strength of response to the strength of texture via Monte Carlo simulation. The sensitivity is limited by systematic errors of the measurement, discussed in Sec. III. Nevertheless, it is instructive to compare sensitivity of this method with other methods; in particular with two point correlators.

The sensitivity of the method is remarkable indeed if one takes into account that statistics in the fifth multiplicity bin for each of the three event generator points is below 3×10^4 events—too scarce, e.g., to extract three source radius parameters via HBT analysis [42] even with a well optimized spectrometer.

The use of two particle correlation in rapidity $R_2(y)$ to search for droplets was discussed for $p\bar{p}$ collisions at $\sqrt{s} = 1.8$ TeV (at FNAL) [32]. R_2 was reported to *decrease* with multiplicity, so that it would not be expected to be visible for dN/dy above ≈ 20; the signal would be *weaker* in a scenario with correlated droplets. In contrast, the wavelet transformation retains sensitivity at high multiplicity, as we see in Fig. 10. In the fifth multiplicity bin, with total number of hadrons at freeze-out around 1.5×10^2, a typical fraction of particles coming from the same fireball for the clustering parameters of 50 (90) would be 3% (6%) [33]. In either case there is little hope of seeing any trace of such dynamics either in ensemble-averaged dN/dy or in dN/dy of a single event, but the systematic difference between the power spectra of the real and mixed events, integrated over multiple

events, nevertheless reveals the difference. The data are consistent with clustering among $\leqslant 3\%$ of the particles.

VI. DISCUSSION

The order of the expected QCD phase transitions is known to be a complex issue for realistic current masses of quarks in the system of a finite size. It is generally expected that a first-order phase transition would be easier to observe. Our dynamic texture measurement tests the hypothesis of the first order phase transition via *QGP droplet hadronization* [4] in a way more direct than interpretation of p_T spectra involving latent heat. Our result can be used to constrain phenomenological quantities which represent basic QCD properties and affect texture formation in this class of hadronization models [4,6,8]. Such quantities are the energy flux, or the rate at which the QGP transmits its energy to hadrons [34,35], the critical size of the QGP droplet [6], and the initial upper energy density of the transition ϵ_0'.

The specific experimental signature of a second-order phase transition (known since the discovery of critical opalescence [36]) is the emergence of critical fluctuations of the order parameter with an enormous increase of the correlation lengths. However, for physical quark masses Rajagopal and Wilczek [12,37] argued that, due to the closeness of the pion mass to the critical temperature, it would be unlikely for the correlation volumes to include large numbers of pions, if the cooling of the plasma and hadronization proceeds in an equilibrated manner. If, on the contrary, the high temperature configuration *suddenly* finds itself at a low temperature, a self-organized criticality regime settles in, and critical local fluctuations develop fully [12,37].

The NA44 data reported here signifies the absence of dynamical fluctuations on the scales probed, within the limit of sensitivity discussed in Sec. V. Convincing evidence of thermal equilibration can be provided by event-by-event observables. Our data are consistent with local thermal equilibrium, which can be understood as an absence of physically distinguished scales between the scale of a hadron and the scale of the system, or the scale invariance of fluctuations [38] (''white noise''). However to *probe* equilibration *directly* with this method, a texture sensitivity at least down to the typical fireball (cluster) sizes observed in pN collisions in cosmic rays and accelerator experiments [39,40] would be necessary. In the absence of such direct evidence, the nonobservation of critical fluctuations can imply either the absence of a second-order phase transition or presence of thermal equilibration—the latter voids the criticality signature, according to Rajagopal and Wilczek [12].

VII. CONCLUSION

We have developed a method of measuring the dynamic components of local fluctuations in charged particle density in pseudorapidity and azimuthal angle, and applied the analysis to Pb+Pb collisions measured by the NA44 experiment. Comparison of the data to a simple Monte Carlo texture event generator indicates that sensitivity to pseudorapidity density clusters involving as few as 3% of the particles is accomplished in this experiment. The probability of encountering a real event whose dynamic azimuthal texture exceeds in strength that of a random mixed event by 3 *RMS*, is below 10%. For the pseudorapidity texture, the respective probability is below 5%. We conclude that this method of event-by-event analysis, sensitive to particular signatures of first- and second-order phase transitions, does not reveal such signatures in 158-GeV/A Pb+Pb collisions at the SPS.

ACKNOWLEDGMENTS

The authors thank N. Antoniou, I. Dremin, K. Rajagopal, E. Shuryak, M. Stephanov, and T. Trainor for illuminating discussions. The NA44 Collaboration thanks the staff of the CERN PS-SPS accelerator complex for their excellent work, and the technical staff in the collaborating institutes for their valuable contributions. This work was supported by the Austrian Fonds zur Förderung der Wissenschaftlichen Forschung, the Science Research Council of Denmark, the Japanese Society for the Promotion of Science, the Ministry of Education, Science and Culture of Japan, the Science Research Council of Sweden, the U.S. Department of Energy, and the National Science Foundation.

[1] N. M. Astafeva, I. M. Dremin, and K. A. Kotelnikov, Mod. Phys. Lett. A **12**, 1185 (1997); I. M. Dremin, O. V. Ivanov, S. A. Kalinin, K. A. Kotelnikov, V. A. Nechitailo, and N. G. Polukhina, Phys. Lett. B **499**, 97 (2001).
[2] H. Appelshauser *et al.*, NA49 Collaboration, Phys. Lett. B **459**, 679 (1999).
[3] R. G. Palmer, Adv. Phys. **31**, 669 (1982).
[4] L. Van Hove, Z. Phys. C **27**, 135 (1985).
[5] L. Van Hove, Z. Phys. C **21**, 93 (1983).
[6] I. Mardor and B. Svetitsky, Phys. Rev. D **44**, 878 (1991).
[7] N. Bilic, J. Cleymans, E. Suhonen, and D. W. von Oertzen, Phys. Lett. B **311**, 266 (1993).
[8] N. Bilic, J. Cleymans, K. Redlich, and E. Suhonen, Z. Phys. C **63**, 525 (1994).
[9] B. Svetitsky and L. Yaffe, Nucl. Phys. **B210**, 423 (1982).
[10] R. Pisarski and F. Wilczek, Phys. Rev. D **29**, 338 (1989).
[11] F. R. Brown, F. P. Butler, H. Chen, N. H. Christ, Z. Dong, W. Schaffer, L. I. Unger, and A. Vaccarino, Phys. Rev. Lett. **65**, 2491 (1990).
[12] K. Rajagopal and F. Wilczek, Nucl. Phys. **B399**, 395 (1993).
[13] M. Stephanov, K. Rajagopal, and E. Shuryak, Phys. Rev. Lett. **81**, 4816 (1998).
[14] E. V. Shuryak and M. A. Stephanov, Phys. Rev. C **63**, 064903 (2001).
[15] J. Barrette *et al.*, E877 Collaboration, Phys. Rev. C **55**, 1420 (1997); C. Pinkenburg *et al.*, E895 Collaboration, Phys. Rev. Lett. **83**, 1295 (1999).
[16] H. Appelshauser *et al.*, NA49 Collaboration, Phys. Rev. Lett. **80**, 4136 (1998).

[17] I. Daubechies, *Ten Lectures on Wavelets* (SIAM, Philadelphia, 1992), p. 129, and references therein.
[18] H. Bøggild *et al.*, NA44 Collaboration, Phys. Lett. B **302**, 510 (1993); **306**, 418 (1993).
[19] E. Beuville, K. Borer, E. Chesi, E. H. Heijne, P. Jarron, B. Lisowski, and S. Singh, Nucl. Instrum. Methods Phys. Res. A **288**, 157 (1990).
[20] L. D. Landau, J. Phys. USSR **8**, 201 (1944).
[21] F. James. MINUIT, Function Minimization and Error Analysis. CERN Program Library Long Writeup D506 (CN Division, CERN, 1994).
[22] The negative autocorrelation introduced thereby between certain channels is immaterial, since our goal is just one effective cross-talk coupling parameter for the detector.
[23] Some authors call this the ''mother function.''
[24] Some authors call it the ''father function.''
[25] J. Pando and L. Z. Fang, Phys. Rev. E **57**, 3593 (1998); L. Z. Fang and J. Pando, astro-ph/9701228.
[26] In our notation, a scalar product of f and g in the $L^2(\mathbb{R}^2)$ space is denoted as $\langle f,g\rangle$: $\langle f,g\rangle=\int\int f(x,y)g(x,y)dxdy$. Repeated indices are being summed over, even if the summation symbol is not written explicitly.
[27] G. Uytterhoeven *et al.*, WAILI: Wavelets with Integer Lifting. TW Report 262, Department of Computer Science, Katholieke Universiteit Leuven, Belgium, July 1997.
[28] P. G. Jones for the NA49 Collaboration, Nucl. Phys. **A610**, 188c (1996).
[29] N. Wiener, *Generalized Harmonic Analysis, and Tauberian Theorems* (MIT Press, Cambridge, MA, 1966), p. 116.
[30] H. Sorge, Phys. Rev. C **52**, 3291 (1995); we use version 2.4 of RQMD.
[31] J. D. Bjorken, Phys. Rev. D **27**, 140 (1983).
[32] P. V. Ruuskanen and D. Seibert, Phys. Lett. B **213**, 227 (1988).
[33] The fireball multiplicity has to be compared, of course, not with $dN/d\eta$, but with the total multiplicity of the event, whose very rough estimate is $3/2\int d\eta dN_{ch}/d\eta=3/2\int dy dN_{ch}/dy$, and if one approximates dN_{ch}/dy with a Gaussian whose σ parameter is 1.4 (based on Ref. [28]), the latter integral is $\approx 5\max(dN/d\eta)$.
[34] B. Banerjee, N. K. Glendenning, and T. Matsui, Phys. Lett. B **127**, 453 (1983).
[35] B. Müller and J. M. Eisenberg, Nucl. Phys. **A435**, 791 (1985).
[36] M. Altschul, Z. Phys. Chem. **11**, 578 (1893); K. von Wesendonck, Naturwiss. Rundsch. **9**, 210 (1894).
[37] K. Rajagopal and F. Wilczek, Nucl. Phys. **B404**, 577 (1993).
[38] T. A. Trainor, hep-ph/0001148.
[39] G. Cocconi, Phys. Rev. **111**, 1699 (1958).
[40] D. Drijard *et al.*, Nucl. Phys. **B155**, 269 (1979).
[41] GEANT—Detector Description and Simulation Tool, CERN Program Library Long Writeup W5013 (CN Division, CERN, 1993).
[42] HBT—two particle interferometry technique, originally due to R. Hanbury Brown and R. Q. Twiss. For a recent review, see U. Heinz and B. V. Jacak, Annu. Rev. Nucl. Part. Sci. **49**, 529 (1999).